



Original Paper

# Characteristics and Evolution of Low-Rank Coal Pore Structure Around the First Coalification Jump: Case Study in Southeastern Junggar Basin

TengFei Jia,<sup>1,2,3</sup> Songhang Zhang,<sup>1,2,3,5</sup> Shuheng Tang,<sup>1,2,3</sup> Meng Wang,<sup>4</sup> Di Xin,<sup>1,2,3</sup> and Qian Zhang<sup>1,2,3</sup>

Received 9 March 2022; accepted 11 June 2022  
Published online: 29 June 2022

The Junggar Basin, which is rich in high-quality low-rank coal and contains the major coalbed methane (CBM) producing blocks in the west of China, has attracted much attention on low-rank CBM exploration and development in recent years. In this study, a series of experimental tests, including mercury intrusion porosimetry (MIP), maceral analyses, proximate analysis, and low-temperature N<sub>2</sub> isotherm adsorption (LT-N<sub>2</sub>GA), were carried out to analyze the variation characteristics of coal compositions and pore systems around the first coalification jump (FCJ) in the southeastern Junggar Basin. The results showed that the FCJ had a considerable influence on the evolution of low-rank coal including coal composition and pore structure. First, the moisture content and the volatile content tended to decrease, and the fixed carbon content tended to increase with increase in maximum reflectance of vitrinite ( $R_o$ ) around the FCJ. Second, the seepage pores transformed gradually to become adsorption pores; the dominant pore types changed from mesopores to micropores; the pore distribution curve transformed from bimodal form to single peak form. In addition, the Brunauer–Emmett–Teller special surface area ( $S_{BET}$ ) showed a “~ -shaped” trend and Barrett–Joyner–Halenda total pore volume ( $V_{BJH}$ ) showed a “U-shaped” trend with increase in  $R_o$  around the FCJ. There were two types of factors that affected the evolution of low-rank coals’ composition and pore structure around the FCJ. One type was external factors, such as dehydration and compaction, causing the coal to become dense; the other type was internal factors, such as bituminization, causing the pores to be filled. These results revealed the characteristics and evolution of coal reservoirs around the FCJ, which can provide a scientific and reliable basis for future exploitation of CBM.

**KEY WORDS:** The first coalification jump, Pore structure, Fractal dimension, Low-rank coal.

<sup>1</sup>Institute of Energy Resources, China University of Geosciences, Beijing 100083, China.

<sup>2</sup>Key Laboratory of Marine Reservoir Evolution and Hydrocarbon Enrichment Mechanism, China University of Geosciences, Ministry of Education, Beijing 100083, China.

<sup>3</sup>Coal Reservoir Laboratory of National Engineering Research Center of CBM Development & Utilization, China University of Geosciences, Beijing 100083, China.

<sup>4</sup>Key Laboratory of Coalbed Methane Resource & Reservoir Formation Process, China University of Mining & Technology, Ministry of Education, Xuzhou 221008, China.

<sup>5</sup>To whom correspondence should be addressed; e-mail: zhangsh@cugb.edu.cn

## INTRODUCTION

With the advancement of the Paris Agreement and the National 14th 5-year plan, China has committed to achieving the ambitious goals of reaching the “carbon peak” and “carbon neutralization” to prevent the continuous warming of the global climate (Wu et al., 2020; Shi et al., 2021). China is rich in CBM resources ( $3.68 \times 10^{13}$  m<sup>3</sup>), of which low-rank CBM resources account for ~ 40% (Wang

et al., 2017a). In the past, it was generally believed that low-rank CBM had little industrial mining value, but it has been proved to have considerable industrial value with the successful development of low-rank CBM in the Erlian Basin (Yuan et al., 2022) and the Turpan-Hami Basin (Yan et al., 2021). Low-rank CBM in China is distributed mainly in the northeastern and northwestern China; in the latter, it is distributed mainly in the Junggar Basin. The development of low-rank CBM in the Junggar Basin has shown great prospects. The highest daily production of CBM wells in Fukang, a demonstration pilot zone for CBM exploitation in the Junggar Basin, could reach  $1.7 \times 10^4 \text{ m}^3$  (Fu et al., 2016a, 2016b).

Pore systems, as a key indicator of coal reservoir, have a profound effect on the adsorption, desorption, migration, and diffusion of CBM (Xin et al., 2019; Xu et al., 2019; Gao et al., 2021; Li et al., 2021a, 2021b). In recent years, several methods have been used to assess coal pore structure, including conventional methods and fractal theory methods, such as nuclear magnetic resonance (NMR), atomic force microscope (AFM), mercury intrusion porosimetry (MIP), Frenkel–Halsey–Hill (FHH), and Menger fractal models (Zhang et al., 2019; Xu et al., 2019; Hou et al., 2020; Xu et al., 2020; Liu et al., 2020; Li et al., 2021a, 2021b; Gao et al., 2021). Currently, some studies related to pore structure characteristics have been conducted in southeastern Junggar Basin, such as pore development characteristics and heating effects (Li et al., 2020; Yu et al., 2020). However, studies to evaluate reservoir characteristics around the FCJ are insufficient, especially regarding changes of composition and pore structure of low-rank coal around the FCJ.

Coalification is a complex nonlinear change process. Each coalification jump affects the molecular structure and coal composition due to variations in physicochemical properties of the coal (Zhou et al., 2017a, 2017b; Jiang et al., 2019). The FCJ is significant for early coalification (Tao et al., 2018a), and it has a huge impact on gas adsorption capacity of coal by changing the pore structure and coal composition, which ultimately restrict the exploration and development of CBM (Kedzior et al., 2015; Li et al., 2016). Current studies on the FCJ have reached a consensus on the variation in moisture content, which continues to decline after the FCJ (Fu et al., 2016b; Tao et al., 2018a; Xin et al., 2019). However, for the evolution of volatile content, the Brunauer–Emmett–Teller (BET) special

surface area ( $S_{\text{BET}}$ ) and the Barrett–Joyner–Halenda (BJH) total pore volume ( $V_{\text{BJH}}$ ) with  $R_o$ , linear (nonlinear) decreases and increases, two exactly opposite views, have been reported (Fu et al., 2016a, 2016b; Tao et al., 2018b; Jiang et al., 2019; Hou et al., 2020). Therefore, it is crucial to clarify the variation characteristics of pore structure and coal composition around the FCJ, as it will not only help to qualitatively and quantitatively evaluate the characteristics of low-rank coal reservoirs, but it will also enable CBM exploration more effective.

In summary, it is necessary to deepen research on the low-rank coal blocks in the Junggar Basin to understand the control mechanism of the FCJ on coal structure. Here, the pore structures around the FCJ are analyzed quantitatively by series of experiments and by adopting Hodot pore classification (Hodot, 1961), which are expected to provide a scientific basis for accelerating the planning and construction of CBM industry in this region.

## SAMPLES AND METHODS

In this study, the coal samples were taken from the Hutubi, Jiangou, Jiangjunmiao, and Liuhuangou coal mines (Fig. 1), southeastern Junggar Basin. All the samples are from the Jurassic Xishanyao Formation. To ensure accuracy of this study, each fresh coal sample (not less than 4 kg) was packaged and sealed after collection and then sent immediately to the laboratory for the experiments.

All the experiments were carried out by strictly following by the Chinese Standard Method. Coal maceral analyses were performed using an Axio Scope A1 photometer microscope following China National Standards GB/T 6948-2008 and GB/T 8899-2013. Proximate analysis was performed using an XL-2000 muffle furnace following China National Standard GB/T 212-2008. MIP measurements were performed using an AutoPore9500 mercury porosimeter following China National Standard GB/T 21650.1-2008. LT-N<sub>2</sub>GA measurements were taken using a TriStar3020 instrument following China National Standard GB/T 21650.2-2008. The methane adsorption isotherm experiment was performed at the Coalfield Geology Bureau of Guizhou following China National Standard GB/T 19560-2008.

MIP is often used to measure pore structure. Before the experiment, all samples were dried at 60 °C for 24 h and vacuumized. Then, mercury was injected into the samples under the control of a

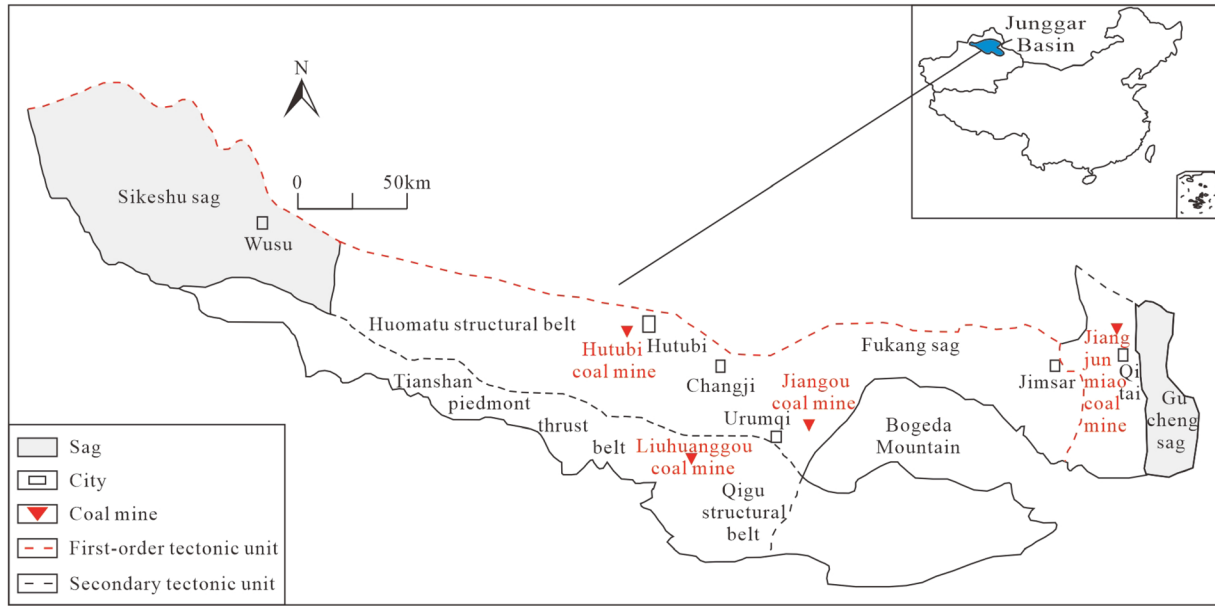


Figure 1. Sample locations in southeastern Junggar Basin.

computer, and some parameters such as intrusion volume, surface area, and pressure were recorded. Constant pressure control was used during the experiments. The maximum intrusion pressure was up to 250 MPa (i.e., 34,000 psi), and the effective pore diameter ranged from 5 to 20,000 nm. Through the intrinsic link between pressure and intrusion mercury, the size of the pores can be expressed as:

$$P = -\frac{2\sigma \cos \theta}{r} \tag{1}$$

where  $P$  represents the mercury injection pressure (MPa),  $\sigma$  represents the surface tension (0.485 N/m) of mercury,  $\theta$  represents the contact angle (130°), and  $r$  represents the pore radius (nm).

Through previous studies using MIP fractal methods by the present authors and other scholars (Liu et al., 2018a, 2018b; 2020; Jia et al., 2021), the Sierpinski model was chosen as the mathematical method for characterizing MIP fractal in this study, thus:

$$\ln(V_1) = \ln \alpha + (3 - D) \ln(P_1 - P_t) \tag{2}$$

where  $V_1$  represents the cumulative injection volume (cm<sup>3</sup>/g),  $\alpha$  represents a constant (dimensionless),  $D$  represents the fractal dimension (dimensionless),  $P_1$  represents absolute injection

pressure (MPa), and  $P_t$  represents the threshold pressure (MPa).

In general,  $D$  is often calculated through an equation and particular the slope  $K_1$  of the logarithmic functions  $\ln(V_1)$  and  $\ln(P_1 - P_t)$ , thus:

$$D_{1,2} = 3 - K_1 \tag{3}$$

Considering that different pressure sections may cause compression of a coal matrix, only the fractal dimension  $D_1$  of macropores (100–20,000 nm) and the fractal dimension  $D_2$  of mesopores (100–1000 nm) were calculated in this study.

LT-N<sub>2</sub>GA is used mainly to measure pores (< 100 nm). Prior to the experiment, samples were ground into a powder and then passed through a 60 mesh sieve. Then, 20–30 g of pulverized coal was collected, dried at 105 °C for 8 h, and outgassed for 16 h. The adsorption/desorption isotherms (0.5–170 nm) were measured with relative pressure (0.05–0.99) at a temperature of 77 K. The BET and BJH models were used to calculate  $S_{BET}$ ,  $V_{BJH}$ , and other parameters.

Due to its wide applicability and ease of understanding, the FHH model was chosen as the mathematical method to describe LT-N<sub>2</sub>GA fractal dimension (Peng et al., 2017; Jia et al., 2021). The FHH model is often defined as

$$\ln V_2 = K_2 \left[ \ln \left( \ln \left( \frac{P_0}{P_2} \right) \right) \right] + C \quad (4)$$

where  $V_2$  represents the volume ( $\text{cm}^3/\text{g}$ ) of adsorbed gases,  $K_2$  represents the slope (dimensionless) of the double logarithm curve,  $P_2$  represents the equilibrium pressure (MPa),  $P_0$  represents the saturation pressure of methane gases (MPa), and  $C$  represents a constant (dimensionless).

Normally, the fractal dimension of the FHH model is often calculated using the following equations:

$$D_3 = 3 + K_2 \quad (5)$$

$$D_4 = 3 + 3 K_2 \quad (6)$$

Considering the different control forces of samples under different relative pressures,  $D_3$  ( $P_2/P_0 > 0.5$ ), which controlled by the capillary condensation regime, and  $D_4$  ( $P_2/P_0 < 0.5$ ), which controlled by the Vander Waals force regime, were calculated. However, many scholars have concluded that  $D_4$  is less than 2 according to Eq. (6), which makes the  $D_4$  meaningless (Zhang et al., 2014; Li et al., 2019; Shao et al., 2020). Due to the lack of specific constraints,  $D_4$  was not discussed further in this study.

The Micromeritics ASAP-2020 analyzer was used to test the methane adsorption properties of the samples. Prior to testing, the samples were crushed and then passed through a 60–80 mesh sieve, and the pulverized coal (around 20 g) was dried at 378.15 °K for 12 h and placed in the sample cylinder. The apparatus was then tested for gas tightness and calibrated for free volume by He. After degassing, the samples were tested for methane adsorption according to the pressure conditions required for the test, with an equilibration time of 12 h for each test point.

## RESULTS AND DISCUSSION

### Basic Physical Properties of Coal

The molecular structure and material composition of coal change with coalification, affecting its pore structure. The different basic physical parameters of the studied samples are given in Table 1. According to previous studies on the FCJ, scholars generally believed that the FCJ occurs when the  $R_o$  is between 0.5 and 0.6%. In this study,  $R_o$  ranged

between 0.55 and 0.86%, elucidating that the samples were around the FCJ. The coal samples' macerals were dominated by vitrinite (62.86–77.49%), followed by inertinite (14.18–32.57%), and liptinite (4.60–6.10%). Every sample had more vitrinite than inertinite and liptinite. In addition, the samples have characteristics of low to high moisture content (2.34–16.73%), low ash yield (3.10–5.19%), and high volatile content (25.97–41.01%). Per the adsorption capacity test, the samples have good adsorption capacity (air-dried Langmuir volumes ( $V_L$ , 6.50–14.75  $\text{m}^3/\text{t}$ )). However, it has a low air-dried Langmuir pressure ( $P_L$ , 0.40–3.40 MPa), which leads to a low critical desorption pressure. Overall, it is not beneficial for CBM development but favorable for gas preservation (Yang et al., 2019; Yu et al., 2020). The FCJ will change the coal composition greatly because of the decrease in enriched oxygen functional groups (such as hydroxyl and carboxyl), the stripping of side chains and some aliphatic functional groups, and the emergence of bitumen (Hoffmann et al., 2012).

### Pore Structure

#### MIP Analysis

The data and parameters measured by the MIP experiment are shown in Table 2. The total intrusion volumes of 1<sup>#</sup> and 4<sup>#</sup> were provided mainly by seepage pores (51.4–80.2%) while those of 2<sup>#</sup>, 3<sup>#</sup>, and 5<sup>#</sup> were provided mainly by adsorption pores (58.4–91%). However, the variation in total intrusion volume of the samples can reach an order of magnitude, with almost a six-fold difference. Therefore, the characteristics of pore structure cannot be analyzed only according to the proportion of relative pores. Moreover, the samples' mercury extrusion efficiency was relatively moderate (8.6–53.2%), indicating that the samples were developed with relatively closed and semi-closed micropores and some transition pores (Wang et al., 2017a, 2017b).

As can be seen from Figure 2a and b, the morphological characteristics of mercury intrusion/extrusion curves of samples were different, but all samples showed the hysteresis loop, which can be classified into three types (Zhu et al., 2016; Wei et al., 2019). Type I (1<sup>#</sup>, 4<sup>#</sup>, and 5<sup>#</sup>) had a continuous increase in accumulation volume at low pressure and the hysteresis loop was very obvious, but the mer-

**Table 1.** Coal maceral, proximate analysis, and basic physical parameters of samples

Sample	$R_o$ (%)	Coal macerals (%)			Proximate analysis (%)				Porosity (%)	Methane isothermal adsorption	
		$V$	$L$	$I$	$M_{ad}$	$A_d$	$V_{daf}$	$FC_d$		$V_L$ (m <sup>3</sup> /t)	$P_L$ (MPa)
1 <sup>#</sup>	0.86	62.86	4.56	32.57	9.64	3.87	25.97	77.16	14.29	6.50	0.40
2 <sup>#</sup>	0.55	73.89	7.93	14.18	2.81	5.19	41.01	55.93	5.47	14.75	3.02
3 <sup>#</sup>	0.78	74.62	8.53	16.85	2.34	3.1	31.64	66.24	6.37	13.59	1.15
4 <sup>#</sup>	0.62	66.74	6.49	26.78	16.73	3.91	33.06	64.33	21.16	12.69	0.46
5 <sup>#</sup>	0.8	77.49	7.22	15.29	5.32	2.52	28.82	69.39	9.37	8.43	3.40

$V$  vitrinite content (%),  $L$  liptinite content (%),  $I$  inertinite content (%),  $R_o$  the maximum reflectance of vitrinite (%),  $M_{ad}$  moisture content (air-dried basis) (%),  $A_d$  ash yield (dry basis) (%),  $V_{daf}$  volatile content (dry, ash free basis) (%),  $FC_d$  fixed carbon content (dry basis) (%),  $V_L$  Langmuir volume (m<sup>3</sup>/t),  $P_L$ , Langmuir pressure (MPa)

**Table 2.** Pore parameters derived from MIP

Sample	$D_{r1}$ (nm)	$V_{in}$ (cm <sup>3</sup> /g)	$V_{out}$ (cm <sup>3</sup> /g)	$E_{ex}$ (%)	$V_1$ (%)	$V_2$ (%)	$V_3$ (%)	$V_4$ (%)	$P_t$ (psi)	100–1000 nm		1000–20,000 nm	
										$D_2$	$R^2$	$D_1$	$R^2$
1 <sup>#</sup>	29.6	0.1148	0.0291	25.3	13.1	38.3	30.8	17.9	10.41	2.4641	0.99	2.7697	0.98
2 <sup>#</sup>	17.5	0.0324	0.0172	53.2	5.2	3.8	48.1	42.9	29.65	2.9827	0.52	2.9948	0.80
3 <sup>#</sup>	17.6	0.0459	0.0242	52.7	8.7	9.7	48.4	33.2	46.04	2.8487	0.96	2.9430	0.94
4 <sup>#</sup>	69.8	0.1784	0.0153	8.6	32.9	47.3	12.3	7.5	61.55	0.7216	0.96	2.7819	0.94
5 <sup>#</sup>	25.6	0.0685	0.0225	32.8	17.2	24.3	38.2	20.2	12.43	2.6736	0.98	2.7488	0.98

$D_{r1}$  average pore diameter, nm;  $V_{in}$  total intrusion volume, cm<sup>3</sup>/g;  $V_{out}$  total extrusion volume, cm<sup>3</sup>/g;  $E_{ex}$  extrusion efficiency (%);  $V_1$  content of macropores (> 1000 nm) (%);  $V_2$  content of mesopores (100–1000 nm) (%);  $V_3$  content of transition pores (10–100 nm) (%);  $V_4$  content of micropores (< 10 nm) (%);  $D_2$  fractal dimension (dimensionless) with pore diameter of 100–1000 nm;  $D_1$  fractal dimension (dimensionless) with pore diameter of 1000–20,000 nm

cury extrusion efficiency was low, indicating that the pore throat of the samples was relatively poor and complex, and many macroscopic bottleneck pores existed, but had relatively good pore connectivity (Wang et al., 2017a, 2017b; Jiang et al., 2019). Type II (3<sup>#</sup>) had a relatively high mercury extrusion efficiency at high pressure compared to type I, indicating that the large size pore of 3<sup>#</sup> had better connectivity with pore throat structure, i.e., relative uniform pore throat size, and that macropores had good connectivity while micropores had poor connectivity. Type III (2<sup>#</sup>) had an insignificant hysteresis loop and a very high mercury extrusion efficiency compared to type II, indicating that the pore system of 2<sup>#</sup> had the best structure, but relatively poor connectivity between macropores and micropores. In addition, the pore size distribution (PSD) showed different characteristics because 1<sup>#</sup> and 4<sup>#</sup> consisted mainly of macropores and mesopores while 2<sup>#</sup>, 3<sup>#</sup>, and 5<sup>#</sup> consisted mainly of micropores and transition pores (Fig. 2c–g). In addition, the pore area distribution (PAD) were all dominated by micropores.

Generally speaking, coal is a relatively soft material with low Young’s modulus and high Poisson’s ratio. Excessive pressure will cause the compressibility of internal pores and fractures to be changed or even destroyed. Some scholars believe that there is a yielding point in the MIP experiment (Fu et al., 2017), where the mercury intrusion rate is smooth before the yielding point and changes suddenly after the yielding point. A coal sample will be compressed and destroyed when the intrusion pressure exceeds the yielding point. As shown in Figure 2a, the mercury accumulation volume changed greatly at pressures of > 1.1 MPa. (Pore diameter was about 800–950 nm.) At present, there are mainly two explanations: The first is that the pores themselves were very developed under the pressure condition, and the second is that the original pores were compressed rapidly under the pressure condition because low-rank coal is softer than high-rank coal. A slight difference can be seen in Figure 2b, in which the coal matrix began to compress at a pressure exceeding 13 MPa (pore diameter was about 100 nm). This was mainly due to the heterogeneity



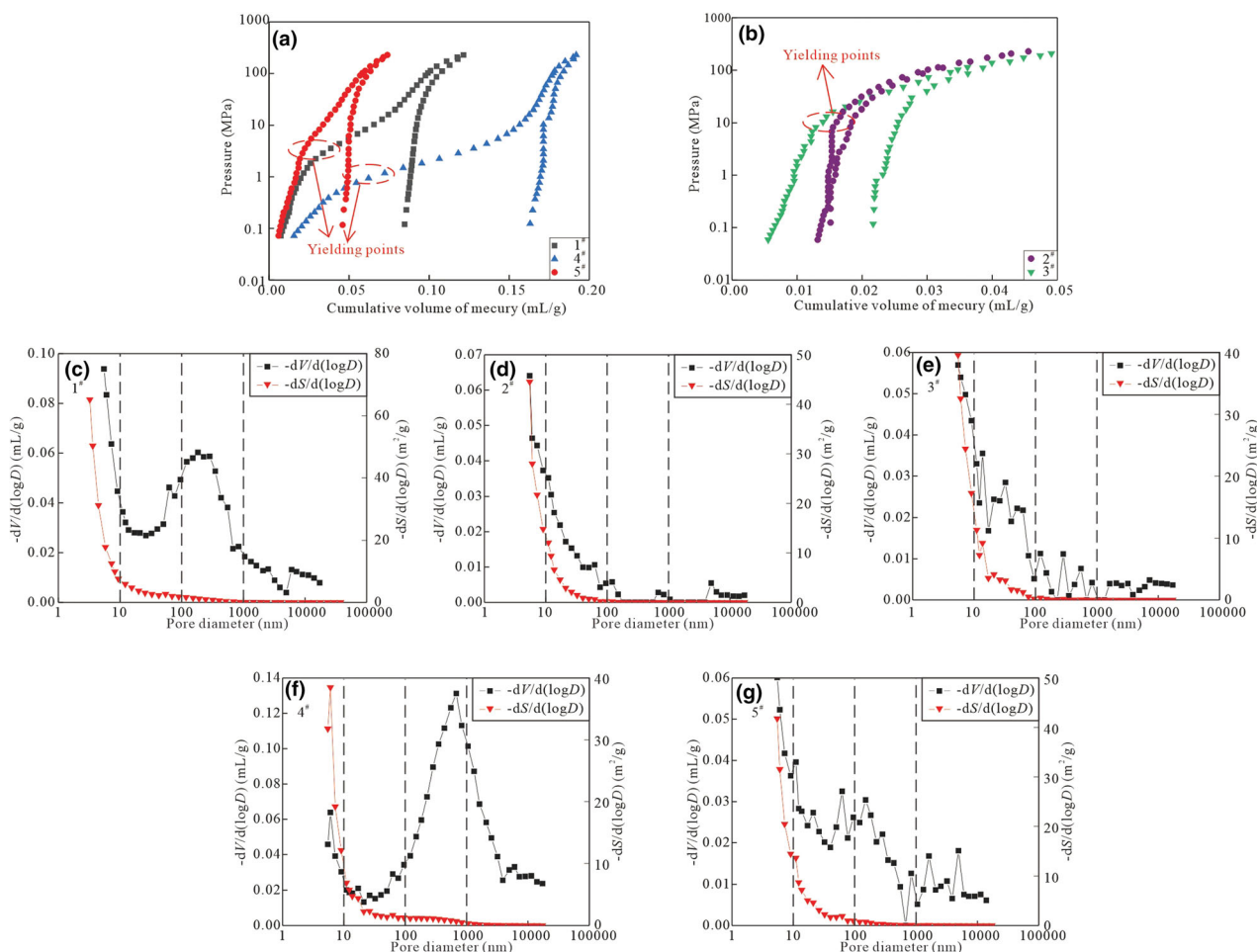


**Figure 2.** Basic parameters of the MIP. Yielding points under (a) low pressure and (b) high pressure. (c), (d), (e), (f), and (g) Distribution curves of pore size and area.

of high moisture coal and the compression of micropores and transition pores, but scholars have not yet reached a consensus (Zhou et al., 2017a, 2017b; Yu et al., 2018; Sun et al., 2020; Li et al., 2021a, 2021b). Therefore, to avoid controversy, the MIP measurements were used only for the macropores characterization in this study, and the results of the remaining tests were used as supplements.

#### LT-N<sub>2</sub>GA Analysis

The results of the LT-N<sub>2</sub>GA experiment calculated by the BET and BJH models are shown in Table 3. The  $S_{\text{BET}}$  and  $V_{\text{BJH}}$  of the samples ranged from 0.4050 to 11.5745 m<sup>2</sup>/g and from 0.001634 to

0.007511 cm<sup>3</sup>/g, respectively. The pore volumes of samples 1<sup>#</sup> and 5<sup>#</sup> were mainly from micropores (48.37–51.51%) and those of samples 2<sup>#</sup>, 3<sup>#</sup>, and 4<sup>#</sup> were mainly from transition pores (63.92–65.73%).

As shown in Figure 3a–c, the adsorption/desorption curves were not the same for different samples, but all of them showed the hysteresis loop phenomenon. In this study, the adsorption/desorption curves were classified into three types and all the N<sub>2</sub> isotherms had similar shapes and represent Type IV isotherms, according to the IUPAC classification criteria (Brunauer et al., 1940; Sing et al., 1985). Type I (samples 2<sup>#</sup>, 3<sup>#</sup>, and 4<sup>#</sup>) showed a narrow hysteresis loop with overlapping isotherms at relative pressure ( $P_2/P_0$ ) between 0 and 0.5, indicating that type I consisted mainly of parallel plate

**Table 3.** Pore parameters derived from LT-N<sub>2</sub>GA

Sample	$S_{BET}$ (m <sup>2</sup> /g)	$V_{BJH}$ (cm <sup>3</sup> /g)	$D_{r2}$ (nm)	Pore volume percentage (%)			$P_2/P_0 > 0.5$	
				> 100 nm	10–100 nm	< 10 nm	$D_3$	$R^2$
1 <sup>#</sup>	11.5745	0.007511	2.5957	9.12	39.37	51.51	2.9198	0.99
2 <sup>#</sup>	0.4050	0.001634	16.1330	17.47	65.73	16.49	2.5249	0.99
3 <sup>#</sup>	0.9781	0.003236	13.2363	15.37	63.92	20.71	2.5423	0.98
4 <sup>#</sup>	1.4702	0.004875	13.2625	15.01	65.58	19.41	2.5674	0.99
5 <sup>#</sup>	4.1404	0.004551	4.3964	9.20	42.43	48.37	2.8369	0.98

$S_{BET}$  BET special surface area (m<sup>2</sup>/g);  $V_{BJH}$  BJH total pore volume (cm<sup>3</sup>/g);  $D_{r2}$  average pore diameter (nm);  $D_3$  fractal dimension (dimensionless) with  $P_2/P_0$  ranging from 0.5 to 1

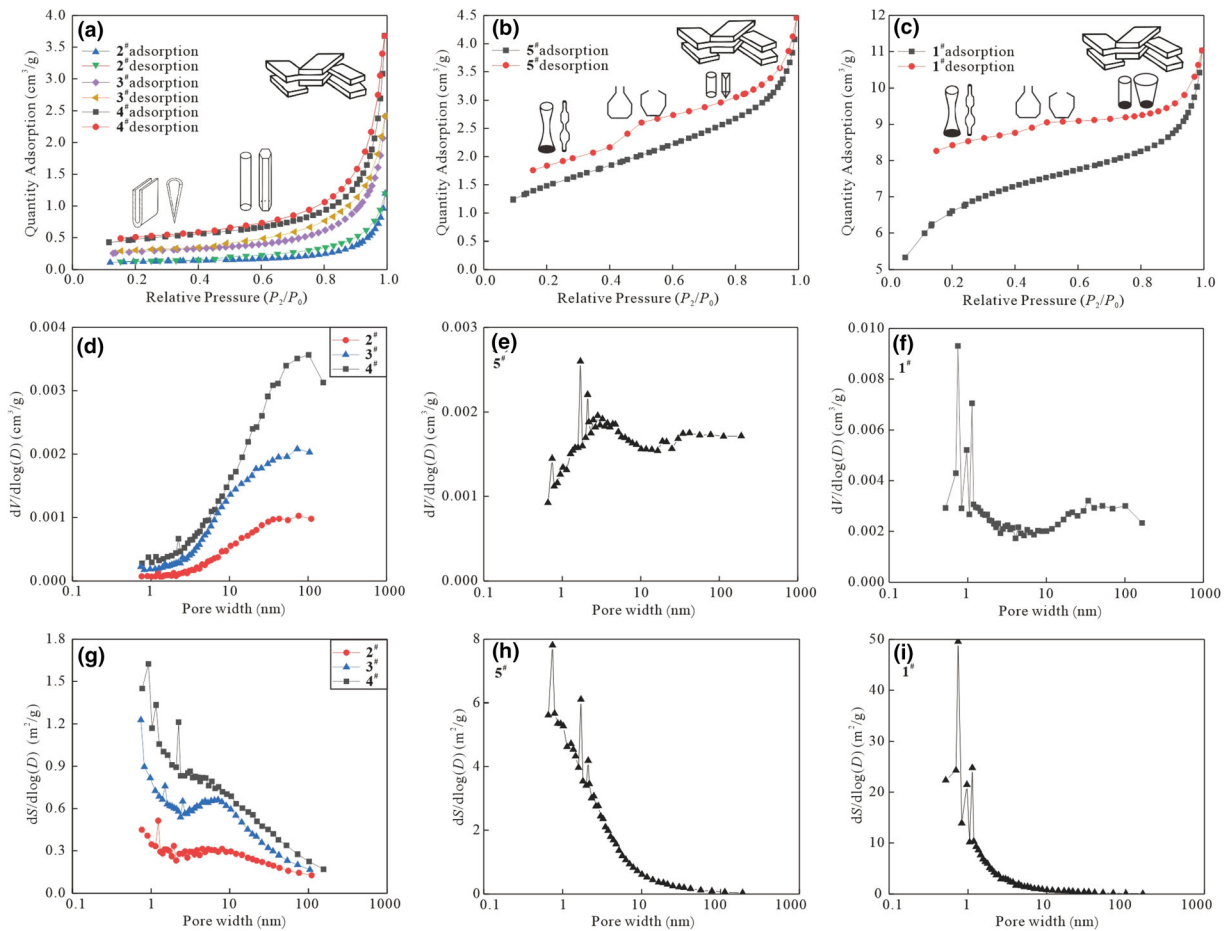


**Figure 3.** Basic parameters of LT-N<sub>2</sub>GA. (a), (b), and (c) N<sub>2</sub> adsorption/desorption curves. (d), (e), and (f) Distribution curves of  $V_{BJH}$ . (g), (h), and (i) Distribution curves of  $S_{BET}$ .

pores (closed at one end) and wedge-shaped pores. The adsorption curve mainly showed a middle section that rose slowly and an end section that rose sharply, indicating the existence of a certain amount of transition pores and mesopores. Type II (sample

5<sup>#</sup>) showed a visible yield point when the  $P_2/P_0$  was about 0.45, which is typical of hysteresis loop phenomenon due to ink-bottle-shaped pores, and the adsorption curve was smoother than type I, indicating that there was few micropores. The difference

between type III (sample 1<sup>#</sup>) and type II is that the yield point was not obvious for the former. In general, ink-bottle-shaped pores are favorable for CBM enrichment, and parallel plate pores are conducive to seepage. Moreover, as can be seen in Figure 3d–f, despite the differences in  $V_{\text{BJH}}$  distribution,  $S_{\text{BET}}$  distribution all have the largest contribution from micropores.

### Relationship Between Fractal Dimensions and Different Compositions

#### *Seepage Pores and Seepage Characteristics*

Considering the heterogeneity and compressibility discussed above for the MIP results, this study only analyzed  $D_1$  in detail according to the Sierpinski fractal model, and  $D_2$  was not discussed to avoid unnecessary controversy. As shown in Figure 4 and Table 2, all  $D_1$  were  $< 3$  (ranging from 2.7488 to 2.9948). Generally speaking, according to many previous studies, the range of fractal dimensions is between 2 and 3 (Zhou et al., 2017a, 2017b; Wang et al., 2018). The closer  $D_1$  is to 3, the more complex is the sample structure; if  $D_1$  is  $> 3$ , the coal matrix can be compressed.

Coalification is the result of a combination of physical and chemical actions. As can be seen from Figure 5a and b, with increase in  $R_o$ , the volatile content showed a decreasing trend whereas the fixed carbon content showed an increasing trend, indicating that  $D_1$  decreased with increasing  $R_o$ . In terms of the evolution of the pore system, the macropores content decreased and the micropores content increased due to increased compaction and dehydration. Figure 5a shows that the complexity of the macropores decreased with coalification. This is mainly due to the compaction and dehydration, which led to the reduction in the macropores content as well as the complexity of the pore structure. In addition, Figure 5b shows that the volatile content and fixed carbon content had positive and negative correlations, respectively, with  $D_1$ . The main reason for this is aromatization in low-rank coals, followed by the oxygen-rich functional groups separation with the generation of  $\text{CO}_2$ ,  $\text{CH}_4$ , and  $\text{H}_2\text{O}$  (Yue et al., 2019), resulting in decrease of  $D_1$ .

The ash yield of coal is often associated with the minerals content of coal. The pore and fracture system of a coal matrix is filled easily by minerals, aggravating the heterogeneity and irregularity of

pore morphology and increasing the fractal dimension (Xie et al., 2019; 2020). Figure 5c also indicates that the surface roughness and pore complexity increase with increase in the ash yield rate as other researchers proved (Yao et al., 2008; Wang et al., 2018; Ren et al., 2019). The influence of moisture content and ash yield are different on pore structure but they have similar effects (Zhang et al., 2009). When moisture content is low, it can fill the pores and increase the heterogeneity; when moisture content is high, its influence is homogenized in the pores, which reduces  $D_1$  (Shao et al., 2020). Physical coalification is the main process in the early coalification stage that alters the pore structure system, specifically in terms of compaction and dehydration. As a result, the moisture content continues to drain and the heterogeneity of coal increases with coalification, thus increasing  $D_1$ . Finally,  $D_1$  increases as the vitrinite content increase and inertinite content decrease (Fig. 5e–f). Generally speaking, the pores of vitrinite are usually smaller than those of inertinite (Li, 2016). Therefore, the pores of inertinite are first compacted with coalification, resulting in the decrease of  $D_1$ . Second, because the pores of vitrinite are mostly micropores, the distribution of the pore volume becomes more complex per unit volume with increase in vitrinite content, causing an increase in  $D_1$ .

#### *Adsorption Pores and Adsorption Characteristics*

The curve for calculating  $D_3$  was divided into two segments (Fig. 6). As seen in Table 3, all  $D_3$  were  $< 3$  (ranging from 2.5249 to 2.9198). Based on the previous analysis, it can be concluded that monolayer adsorption (mainly at the lower relative pressure stage), multilayer adsorption (continuous adsorption after the monolayer adsorption is saturated), and capillary condensation (mainly at the higher relative pressure stage) existed at the same time.

$D_3$  shows a positive relationship with  $R_o$  (Fig. 7a), indicating that the internal structure of pores became more complex with coalification, while the transition pores and mesopores ( $P_2/P_0 > 0.5$ ) kept increasing with the transformation of macropores. As shown in Figure 7b,  $D_3$  was positively correlated with fixed carbon content and negatively correlated with volatile content. The different relationships of  $D_3$  and  $D_1$  with coal industrial analysis parameters suggest that coal rank affects



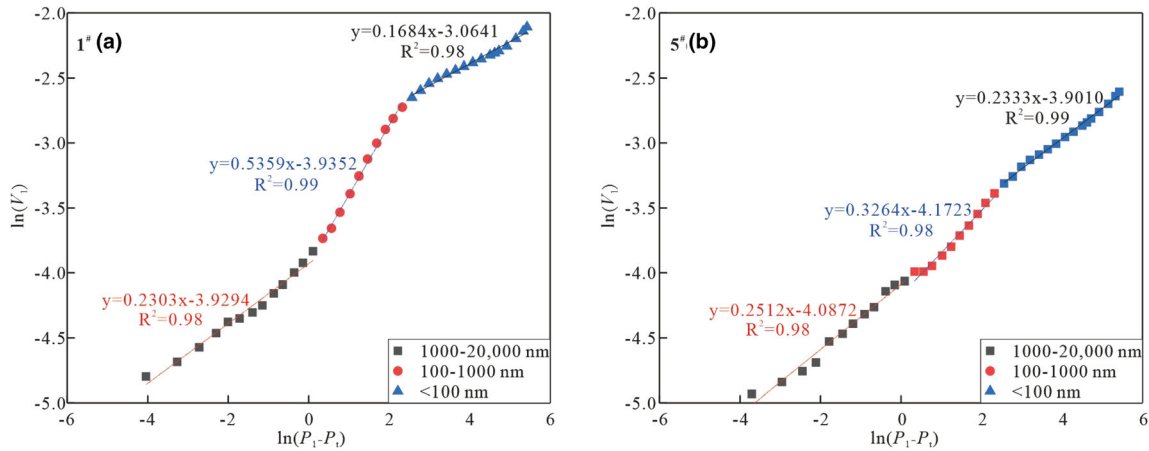


Figure 4. Fractal dimension characteristics of samples per the Sierpinski model: (a) sample 1#; (b) sample 5#.

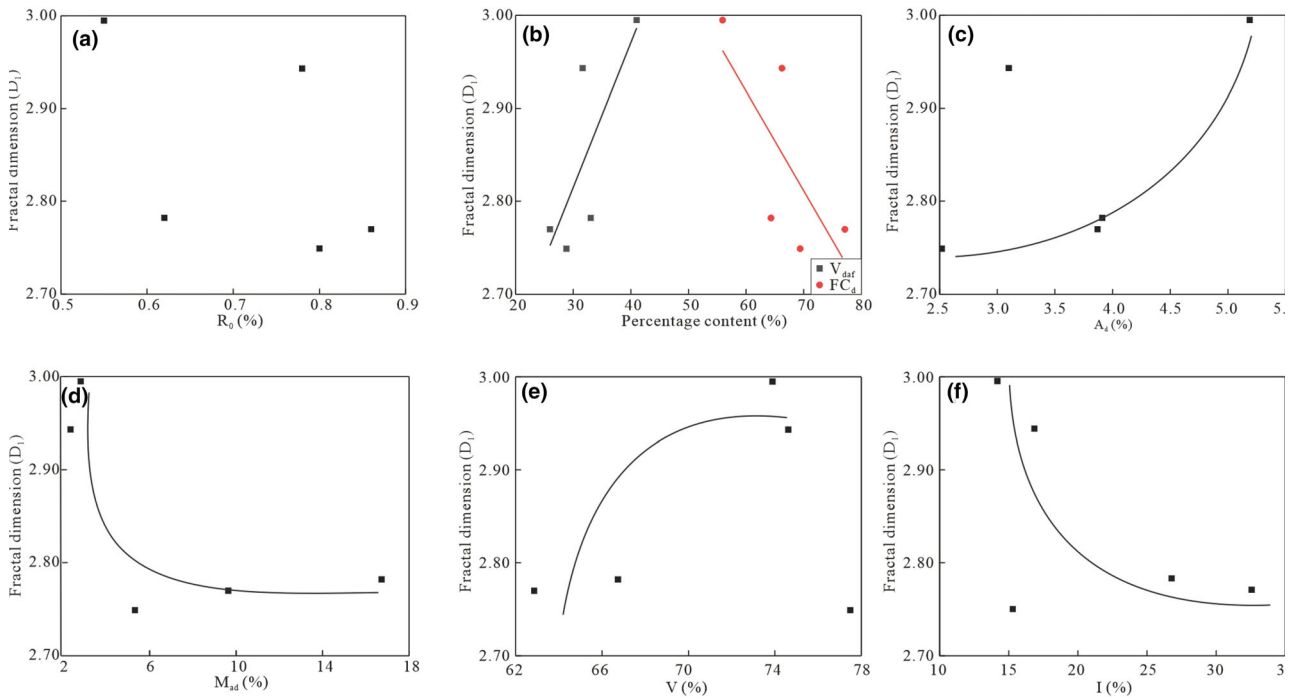
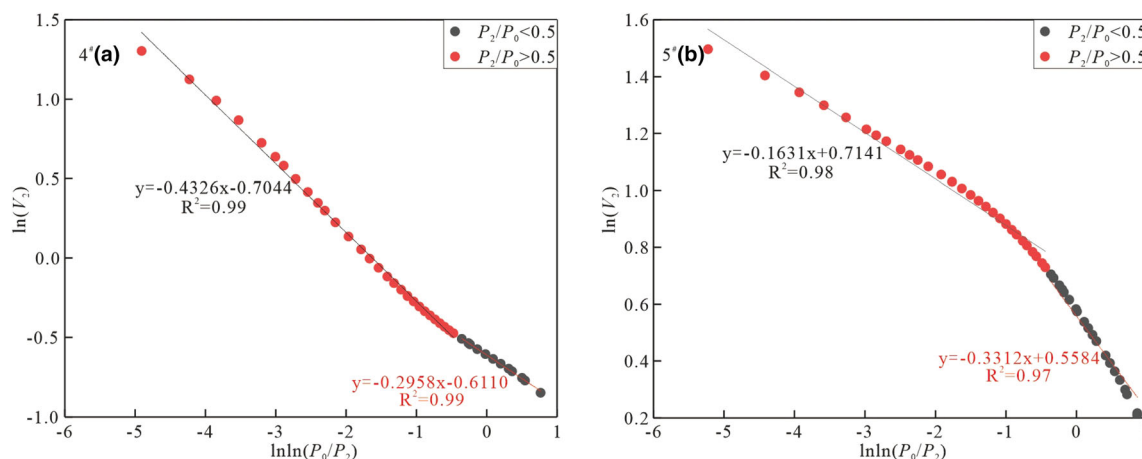


Figure 5. Relationships of  $D_1$  with different parameters. (a) Maximum vitrinite reflectance. (b) Volatile content and fixed carbon content. (c) Ash yield. (d) Moisture content. Change trends of (e) vitrinite and (f) inertinite.

pore structure more than coal composition, such as volatile and fixed carbon content. In addition, devolatilization gradually loses its dominance with fixed carbon content increases. Instead, transition pores and micropores vary differently, with the former decreasing in content and the latter increasing in content. A higher proportion of micropores leads

to a higher fractal dimension of coal with higher fixed carbon content (Chen et al., 2011). As shown in Figure 7c, compared with the vitrinite and inertinite contents, the correlation of  $D_3$  with liptinite content was not significant. Inertinite and vitrinite contents had different effects on  $D_3$  (Fig. 7d-e). According to the different formation of inertinite and vitrinite



**Figure 6.** Fractal dimension characteristics of the FHH model based on adsorption branch: (a) sample 4<sup>#</sup>; (b) 5<sup>#</sup> sample.

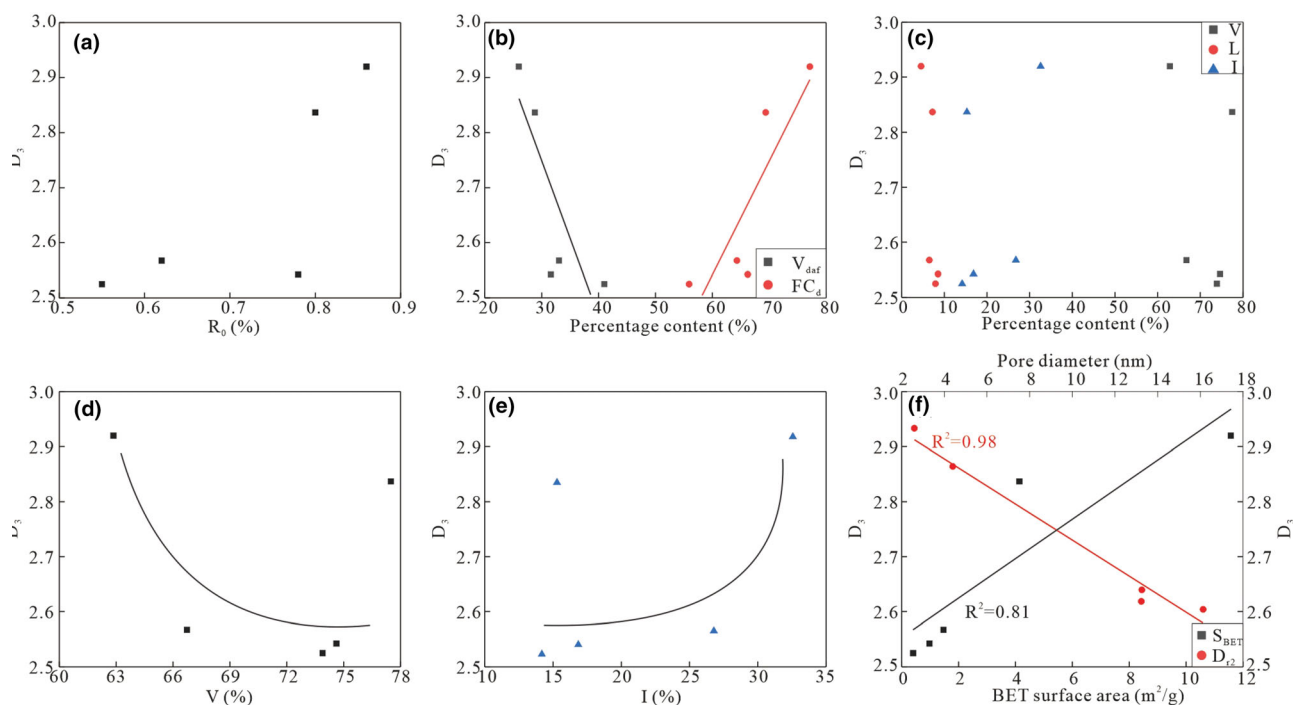


**Figure 7.** Relationships of  $D_3$  with different parameters. (a) Maximum vitrinite reflectance. (b) Volatile content and fixed carbon content. (c) Vitrinite, liptinite, and inertinite contents. Change trends of (d) vitrinite and (e) inertinite. (f)  $S_{\text{BET}}$  and  $D_{12}$  content.

(carbonization and gelation, respectively), the former has some aromatic structure in the early stages of coalification, and the latter increases with coalification (Liu et al., 2021). The most important change in vitrinite is the increase in condensation of aromatic rings (Xin et al., 2019). In addition, high vitrinite content creates some gas pores which are

connected to transition pores and micropores, thus reducing the complexity of the pores. Inertinite accounts for a high proportion of transition pores, and the heterogeneity increases with increasing inertinite content (Clarkson et al., 1996).

It should be noted that the main information reflected in the LT- $\text{N}_2$ GA experiment is the content

of transition pores and mesopores. There was a distinct relationship between  $D_3$  and pore structure parameters (Fig. 7f). When  $D_3$  kept increasing, the  $S_{\text{BET}}$  increased ( $R^2 = 0.81$ ) and the  $D_{r2}$  ( $R^2 = 0.98$ ) decreased, indicating that the larger the  $D_3$ , the more adsorption site ( $S_{\text{BET}}$ ), the more conducive the CBM enrichment. Moreover, it is not appropriate to analyze methane adsorption by a single factor. The fractal dimension represents the complexity of coal pore structure. Therefore, the relationships of  $D_3$  with  $V_L$  and  $P_L$  are discussed. As can be seen in Figure 8,  $V_L$  showed a regular variation with decrease in  $D_3$ , indicating that the higher  $D_3$ , the more difficult it is for methane adsorption, which is contrary to the previous conclusion. This situation is affected by two aspects. First, the pores that control the adsorption capacity most are controlled by ultramicropores ( $< 2$  nm), while pores ( $> 2$  nm) do not dominate the adsorption capacity. Second,  $D_3$  is influenced by the surface tension and capillary condensation (Zhou et al., 2016; Li et al., 2018a, 2018b).

### Variable Characteristics of Coal Properties Around the FCJ

#### *Relationships of Composition Characteristics and the FCJ*

To more intuitively compare the changes in the low-rank coal compositions around the FCJ, data from different studies were discussed in this study (Fu et al., 2016a, 2016b; Wang et al., 2017a, 2017b; Zhou et al., 2017a, 2017b; Tao et al., 2018a; Xin et al., 2019; Hou et al., 2020). According to Figure 9, moisture and volatile contents were negatively correlated with  $R_o$ ; fixed carbon content was positively correlated with  $R_o$ ; and ash content had no obvious relationship with  $R_o$ . Generally speaking, the emergence of bitumen is the main indicator of the FCJ. When  $R_o$  is  $< 0.5\%$ , the moisture content is high due to the strong hydrophilicity of coal. It should be clear that the hydrophilicity of low-rank coals comes mainly from the presence of many polar functional group, and vitrinite with rich hydroxyl groups is more hydrophilic than inertinite (Faiz et al., 2007; Duan et al., 2009). When  $R_o$  is  $> 0.6\%$ , the moisture and volatile contents decrease because functional groups (carboxyl, hydroxyl) and side chains (alkyl) are separated and the order of molecular structure gradually increases with coalification. At the same time,  $\text{CH}_4$ ,  $\text{CO}_2$ , and  $\text{H}_2\text{O}$  are

continuously released, leading to a reduction in volatile content. The composition differences of different samples at different coalification stages show that the composition of low-rank coal changed greatly around the FCJ.

It is noteworthy that some samples had abnormally high moisture content after the FCJ (Fig. 9a). Based on Figure 10, there was a clear positive correlation between moisture content and the content of seepage pores. Therefore, it can be inferred that the abnormal moisture content was due to the development of seepage pores, but this phenomenon does not conform to the conventional understanding of the relation between moisture content and adsorption pores.  $M_{\text{ad}}$  refers to the internal moisture of coal, and this moisture is adsorbed or condensed mainly in adsorption pores. There are three likely reasons for the positive correlation. First, although the binding capacity of seepage pores to moisture is weak, the seepage pore content was high and the total pore volume was large, providing more space for the preservation of moisture. Second, the more development of the seepage pore means the greater content of the hydrophilic functional groups at the similar coal rank, which may result in higher moisture content. Third, due to the emergence of bitumen, some pores and throats may be blocked, resulting in the preservation of moisture. However, the relative content of pores cannot be considered solely. Because  $M_{\text{ad}}$  is internal moisture content, the absolute content of adsorption pores should play a decisive role in moisture content. Therefore, taking the data of this study as example, the mercury intrusion volume from samples 1<sup>#</sup> to 5<sup>#</sup> adsorption pores were 0.0294 to 0.0559  $\text{cm}^3/\text{g}$ , the mercury intrusion volume was in the same order of magnitude, and the difference was not very large. In conclusion, the seepage pores had a definite influence on the variation of moisture content.

#### *Relationships of Pore Structure Characteristics and the FCJ*

To clarify further the evolutionary characteristics of different pores around the FCJ, the variations of parameters related to pore structure obtained from the MIP and LT- $\text{N}_2$ GA experiments were analyzed systematically by comparing the results with those in previous studies (Fu et al., 2016a, 2016b; 2017; Wu et al., 2017; Li et al., 2018a, 2018b;

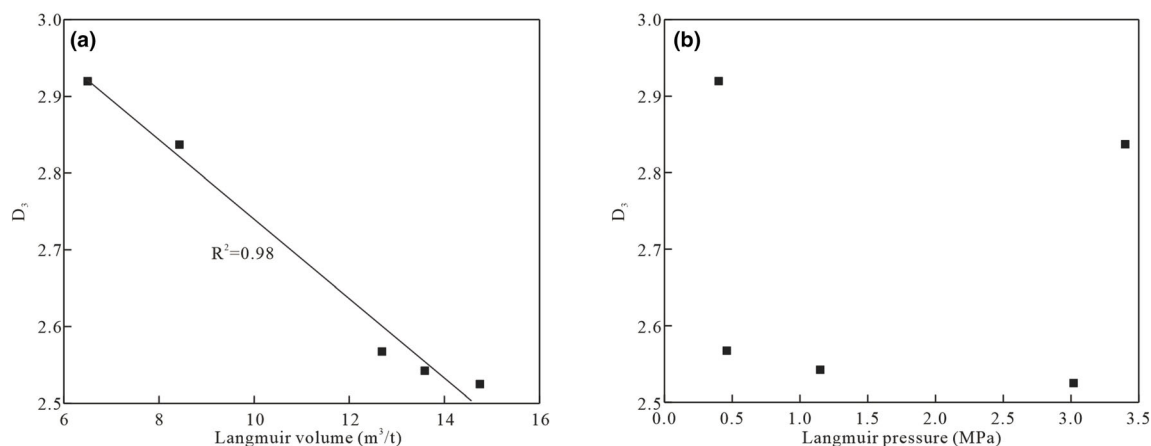


**Figure 8.** Relationships among Langmuir volume, Langmuir pressure, and  $D_3$ . (a)  $D_3$  vs.  $V_L$ . (b)  $D_3$  vs.  $P_L$ .

Tao et al., 2018a, 2018b; Wang et al., 2018; Zhu et al., 2019; Hou et al., 2020; Zhang et al., 2021).

By comparing the results of the MIP experiment with those in previous studies (Fig. 11), it can be concluded that there was a constant conversion of seepage pores to adsorption pores with coalification. In particular, many samples showed a rapid decrease in seepage pores and an increase in adsorption pores when  $R_o$  was  $< 0.6\%$ . This phenomenon occurred with the FCJ, not only because coal with  $R_o$  of  $> 0.6\%$  has greater compaction, but also because of reduced dehydration and increased bituminization, resulting in higher coal density. In addition, compared with the PSD characteristics before and after the FCJ obtained by previous scholar (Tao et al., 2018a), the PSD in this study exhibited different characteristics. As can be seen from Figure 2d, e and g, the pore volume transitioned from the original predominantly mesopores and macropores to the current predominantly micropores and transition pores, and the peak value of pore changed from mesopores to micropores with increase in  $R_o$ . Samples 1<sup>#</sup> and 4<sup>#</sup> had more developed seepage pores because inertinite, which mainly develop mesopores and macropores, was relatively developed in them. Of course, the influence of strong tectonic activity cannot be excluded, which can result in the development of high porosity and more seepage pores. Moreover, the PSD before the FCJ was more uniform (most of the pore distribution showed a bimodal form), but the PSD after the FCJ was more extreme (most of the pore distribution showed a single peak form). Through the variation of the

different pores, it can be seen that the FCJ had a great influence on the development seepage pores.

Comparing the results of LT-N<sub>2</sub>GA experiments with those in previous studies (Fig. 12) revealed that there was no obvious change in the content of mesopores with increase in  $R_o$ , but the content of transition pores decreased and the content of micropores increased. This indicates that coalification has an effect on adsorption pores. A comparison of changes in seepage pores and adsorption pores showed that the FCJ had a stronger effect on seepage pores than on adsorption pores. Moreover, the proportion of different pore types was variable. For example, Tao et al. (2018a) pointed out that little changes in the pore proportion around the FCJ, and the samples were mainly composed of transition pores. However, in other studies, the proportion of mesopores after the FCJ dominate (avg. 31.4%). Fu et al. (2016a, 2016b) reported huge changes in pore proportion before and after the FCJ, and the samples were composed mainly of micropores. When  $R_o$  is  $< 0.5\%$ , the transition pores and micropores can occupy 41.7 and 52.7%, respectively, but when  $R_o$  is  $> 0.6\%$ , the transition pores and micropores can occupy 9.2 and 89.1%, respectively. Generally, this phenomenon is caused by coalification, which leads to the dissociation of aliphatic structures ( $-\text{CH}_3$ ,  $-\text{CH}_2$ , and  $-\text{CH}$ ), the formation of small molecular compounds ( $\text{H}_2\text{O}$ ,  $\text{CO}_2$ , and  $\text{CH}_4$ ) and the separation of functional groups (Liu et al., 2018a, 2018b). In addition, samples have different formation conditions. In particular, a high inertinite content leads to faster condensation of aromatic rings and the development

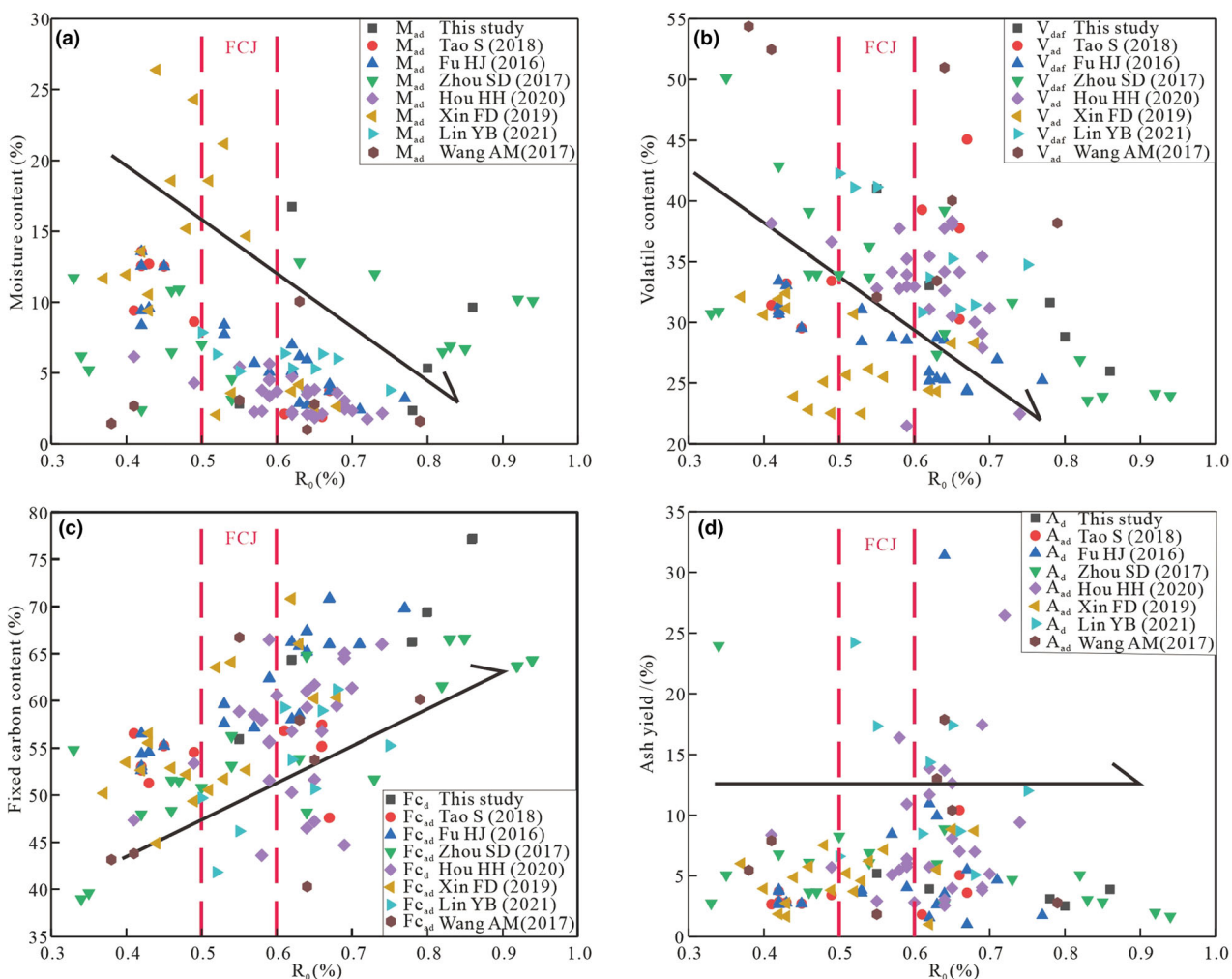


**Figure 9.** Plots of  $R_o$  versus the basic properties of samples. Evolution of (a) moisture content, (b) volatile content, (c) fixed carbon content and (d) ash yield.

of gas pores, and compacted tissue pores in vitrinite result in higher content of micropores.

Previous studies have shown that  $S_{BET}$  and  $V_{BJH}$  first decrease and then increase before and after the FCJ (Jiang et al., 2019). In this study, the results of previous studies were integrated (Fu et al., 2016a, 2017; Li et al., 2017; Wu et al., 2017; Tao et al., 2018a, 2018b; Zhou et al., 2018; Xin et al., 2019; Zhu et al., 2019; Hou et al., 2020; Liu et al., 2020). To obtain the overall change law of  $S_{BET}$  and  $V_{BJH}$  as much as possible, the data with the same  $R_o$  were processed as follows. (1) When there were three or more values, the highest and lowest values were removed, and the remaining values were averaged for use in the analysis. (2) If there were

only two values, their average was used. (3) If there was only one value, this value was used. The results show that  $S_{BET}$  piecewise increased and decreased with coalification, showing a “~ -shaped” trend, and  $V_{BJH}$  first increased and then decreased with coalification, showing a “U-shaped” trend (Fig. 13a, b). In addition, according to the collected data, there were different relationships of  $R_o$  with  $S_{BET}$  and  $V_{BJH}$ , mainly because  $S_{BET}$  and  $V_{BJH}$  are controlled not only by coalification but also by other factors such as coal molecules and macerals. With coalification,  $S_{BET}$  first increased, reached a maximum at a  $R_o$  in the range of 0.5–0.6%, then decreased, reaching a minimum at a  $R_o$  of ~ 0.7%, and finally



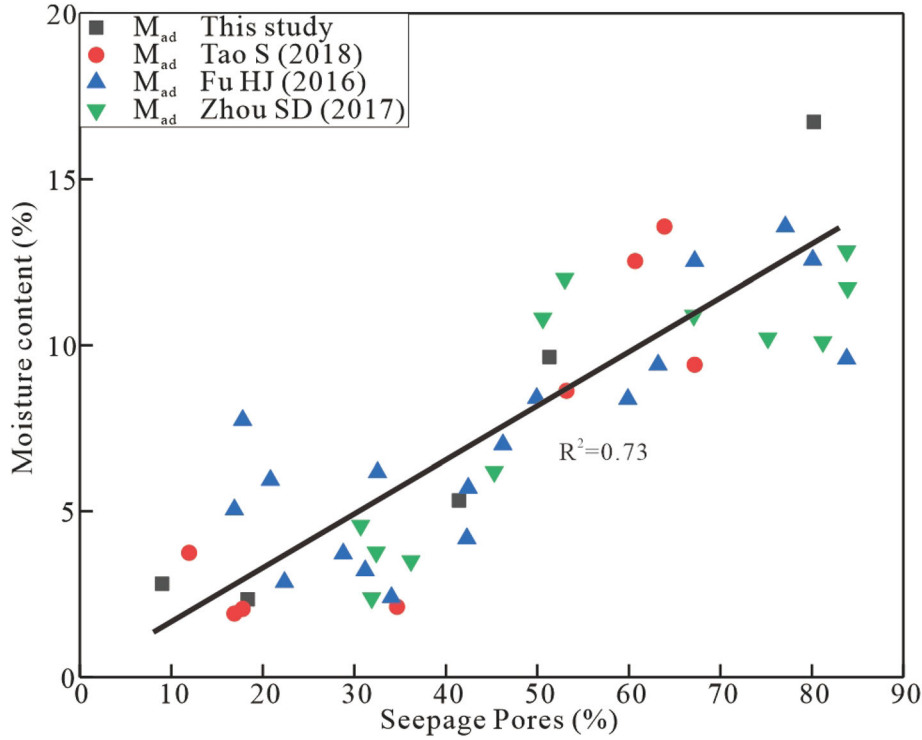


Figure 10. Relationship between moisture and the content of seepage pores.

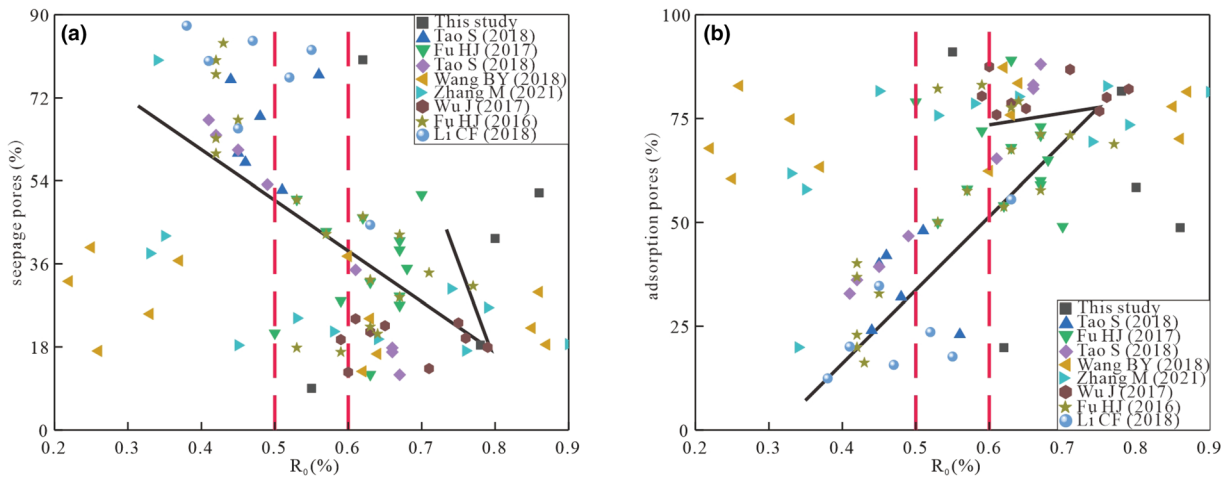
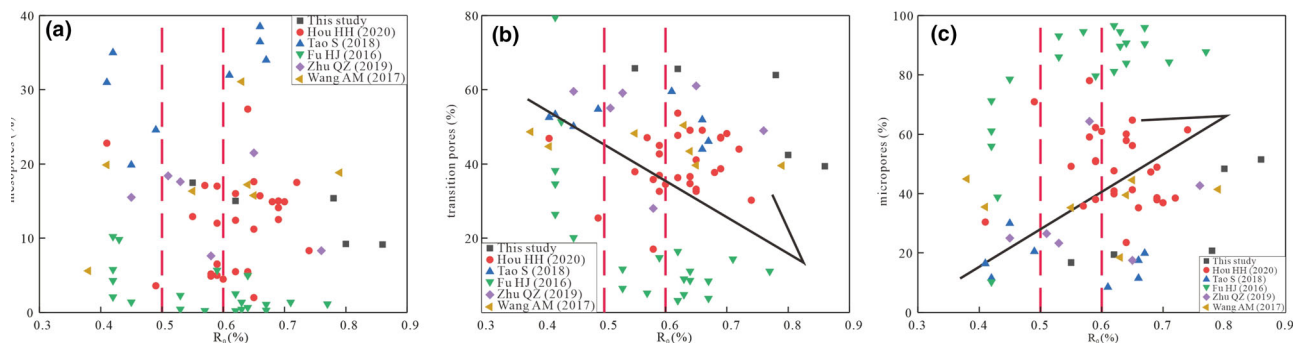


Figure 11. Relationships between pores of samples around the FCJ measured with MIP. Evolution of (a) seepage pores and (b) adsorption pores.

continued to increase.  $V_{BJH}$  first decreased, reaching a peak at  $R_0$  of  $\sim 0.6\%$ , and then increased.

The “ $\sim$ -shaped” change of  $S_{BET}$  is consistent with the changes of pores.  $S_{BET}$  is provided mainly by micropores followed by transition pores. When

$R_0$  is  $< 0.6\%$ , the content of transition pores decreased and the content of micropores increased. In other words,  $S_{BET}$  increased. However, when  $R_0$  was between 0.6 and 0.7%, the change trend in the content of transition pores and micropores was



**Figure 12.** Relationships of pores of samples around the FCJ measured with LT-N<sub>2</sub>GA. Evolution of (a) mesopores, (b) transition pores, and (c) micropores.

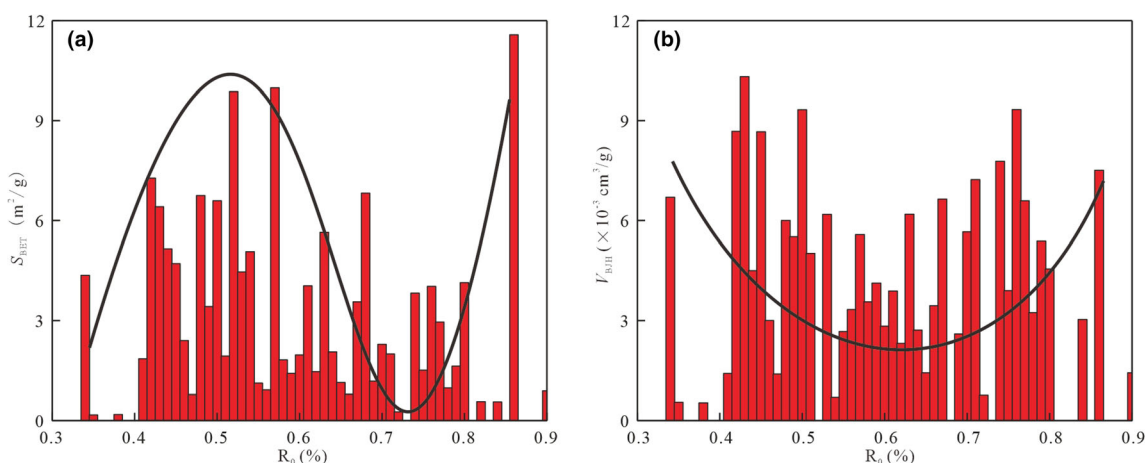


**Figure 13.** Distribution of  $S_{BET}$  and  $V_{BJH}$  of the samples. Schematic diagrams of (a)  $S_{BET}$  and (b)  $V_{BJH}$ .

fuzzy, indicating that the interaction between bituminization and coalification was complex. When  $R_0$  exceeded 0.7%, this trend was similar to the initial state, resulting in a continuous increase of  $S_{BET}$ . Compared with  $S_{BET}$ ,  $V_{BJH}$  is provided mainly by transition pores, followed by mesopores and micropores. Therefore,  $V_{BJH}$  initially increased, then decreased with decrease in the content of transition pores, and finally increased with increase in mesopores and micropores.

In addition, the decrease of  $S_{BET}$  is due to the blocking and filling effect of bitumen and clay minerals, resulting in the reduction of micropores. In particular, the bitumen produced early in the coalification process blocks the pore space of vitrinite or is adsorbed by vitrinite. Then, the following changes occur under the action of high temperature and high pressure with coalification: (1) formation of a small

number of gas pores; (2) some amount of bitumen undergoes thermal degradation at high temperature; and (3) appearance of secondary pores, such as intracrystalline pore and dissolution pore. The joint influence mentioned above eventually leads to increase in  $S_{BET}$ . This regulation is also relatively applicable to  $V_{BJH}$ .

Generally, the evolution of pore structure around the FCJ is not only controlled by external factors such as compaction and dehydration (tectonic action is not excluded), but also by internal factors such as bituminization and devolatilization. However, it is difficult to characterize quantitatively the impact of each factor. In addition, coal has strong heterogeneity, and the previous data used in this study were not all from coal samples in the Junggar Basin. Therefore, only detailed results are obtained on pore structure evolution around the

FCJ, but one cannot quantify accurately the control law of a certain factor in the study area. That is to say, further research is needed on the low-rank coal blocks in the Junggar Basin.

## CONCLUSIONS

- (1) The samples investigated in this study were highly heterogeneous with characteristics of low–high moisture content (2.34–16.73%), low ash yield (3.10–5.19%), and high volatile content (25.97–41.01%). The mercury intrusion/extrusion curves and adsorption/desorption curves of different samples generally showed relatively good pore throat structure and pore connectivity.
- (2) Based on the Sierpinski model and the FHH model, the fractal dimensions  $D_1$  and  $D_3$  were calculated according to MIP and LT-N<sub>2</sub>GA experimental data, respectively. Comparing the changes of  $D_1$  and  $D_3$  with  $R_o$ , coal macerals, and proximate analysis showed that the evolution of coal compositions had a complex and comprehensive influence on the fractal characteristics of pores.  $D_1$  is more easily influenced by physical changes and  $D_3$  is more easily affected by chemical changes.
- (3) The FCJ has a considerable influence on the changes in the coal composition and pore structure. Comparison of research results of different studies showed that both external factors (such as dehydration and compaction) and internal factors (such as the separation of alkyl and functional groups) affect low-rank coal pore structure evolution. Thus,  $S_{BET}$  and  $V_{BJH}$  show a “~ -shaped” and a “U-shaped” change trends with coalification, respectively.

## ACKNOWLEDGMENTS

The project was financially supported by the Key Project of Natural Science Foundation of China (U1903209), the Natural Science Foundation of Autonomous Region (2018D01C062) and the Special Fund for Basic Scientific Research Business Expenses of Central University (2020ZDPYMS09).

## DECLARATIONS

**Conflict of Interest** The authors declare that they have no known competing financial interests or personal relationships that could have appeared to influence the work reported in this paper.

## REFERENCES

- Brunauer, S., Deming, L., Deming, W., & Teller, E. (1940). On a theory of the van der Waals adsorption of gases. *Journal of American Chemical Society*, 62, 1723–1732.
- Chen, Y., Wang, X., & He, R. (2011). Modeling changes of fractal pore structures in coal pyrolysis. *Fuel*, 90, 499–504.
- Clarkson, C. R., & Bustin, R. M. (1996). Variation in micropore capacity and size distribution with composition in bituminous coal of the Western Canadian Sedimentary Basin - implications for coalbed methane potential. *Fuel*, 75, 1483–1498.
- Duan, X., Qu, J., & Wang, Z. (2009). Pore structure of macerals from a low rank bituminous. *Journal of China University of Mining & Technology*, 38, 224–228.
- Faiz, M., Saghafi, A., Sherwood, N., & Wang, I. (2007). The influence of petrological properties and burial history on coal seam methane reservoir characterisation, Sydney Basin, Australia. *International Journal of Coal Geology*, 70, 192–208.
- Fu, H., Tang, D., Xu, H., Xu, T., Chen, B., Hu, P., Yin, Z., Wu, P., & He, G. (2016a). Geological characteristics and CBM exploration potential evaluation: A case study in the middle of the southern Junggar Basin, NW China. *Journal of Natural Gas Science and Engineering*, 30, 557–570.
- Fu, H., Tang, D., Xu, H., Tao, S., Xu, T., Chen, B., & Yin, Z. (2016b). Abrupt changes in reservoir properties of low-rank coal and its control factors for methane adsorbability. *Energy & Fuels*, 30, 2084–2094.
- Fu, H., Tang, D., Xu, T., Xu, H., Tao, S., Li, S., Yin, Z., Chen, B., Zhang, C., & Wang, L. (2017). Characteristics of pore structure and fractal dimension of low-rank coal: A case study of Lower Jurassic Xishanyao coal in the southern Junggar Basin, NW China. *Fuel*, 193, 254–264.
- Gao, X., Wang, Y., Wu, X., Li, Y., Ni, X., & Zhao, S. (2021). Nanoscale pore structure characteristics of deep coalbed methane reservoirs and its influence on CH<sub>4</sub> adsorption in the Linxing area, eastern Ordos Basin, China. *Journal of Nanoscience and Nanotechnology*, 21, 43–56.
- Hodot, B.B. (1961). *Outburst of coal and coalbed gas*. National Mining Scientific and Technical Documentation Press.
- Hoffmann, K., & Huculak-Macaka, M. (2012). The utilization possibility of waste lignite as a raw material in the process of obtaining humic acids preparations. *Polish Journal of Chemical Technology*, 14, 1–6.
- Hou, H., Shao, L., Tang, Y., Zhao, S., Yuan, Y., Li, Y., Mu, G., Zhou, Y., Liang, G., & Zhang, J. (2020). Quantitative characterization of low-rank coal reservoirs in the southern Junggar Basin, NW China: Implications for pore structure evolution around the first coalification jump. *Marine and Petroleum Geology*, 113, 104165.
- Jia, T., Wang, M., Gao, X., Zhao, J., & Zhu, J. (2021). Pore structure characteristics of low-rank coal reservoirs and evaluation of fractal models. *Natural Gas Geoscience*, 32, 423–436.

- Jiang, J., Yang, W., Cheng, Y., Zhao, K., & Zheng, S. (2019). Pore structure characterization of coal particles via MIP, N<sub>2</sub> and CO<sub>2</sub> adsorption: Effect of coalification on nanopores evolution. *Powder Technology*, 354, 136–148.
- Kedzior, S. (2015). Methane contents and coal-rank variability in the Upper Silesian Coal Basin, Poland. *International Journal of Coal Geology*, 139, 152–164.
- Li, T., Wu, C., & Wang, Z. (2020). The dynamic change of pore structure for low-rank coal under refined upgrading pre-treatment temperatures. *Petroleum Science*, 2020, 430–443.
- Li, G. (2016). Coal reservoir characteristics and their controlling factors in the eastern Ordos basin in China. *International Journal of Mining Science and Technology*, 26, 1051–1058.
- Li, W., Zhu, Y., Wang, M., & Jiang, B. (2016). Characterization of coalification jumps during high rank coal chemical structure evolution. *Fuel*, 185, 298–304.
- Li, Y., Song, D., Liu, S., Ji, X., & Hao, H. (2021a). Evaluation of pore properties in coal through compressibility correction based on mercury intrusion porosimetry: A practical approach. *Fuel*, 291, 120130.
- Li, X., Li, Z., Wang, E., Liang, Y., Li, B., Chen, P., & Liu, Y. (2018a). Pattern recognition of mine microseismic and blasting events based on wave fractal features. *Fractals-Complex Geometry Patterns and Scaling in Nature and Society*, 26, 1850029.
- Li, Y., Song, D., Li, G., Ji, X., Tang, J., Lan, F., & Fan, S. (2021b). Applicability analysis of determination models for nanopores in coal using low-pressure CO<sub>2</sub> and N<sub>2</sub> adsorption methods. *Journal of Nanoscience and Nanotechnology*, 21, 472–483.
- Li, Z., Liu, D., Cai, Y., Wang, Y., & Teng, J. (2019). Adsorption pore structure and its fractal characteristics of coals by N<sub>2</sub> adsorption/desorption and FESEM image analyses. *Fuel*, 257, 116031.
- Li, C., Wei, Y., Wang, A., & Cao, D. (2018b). Low-rank coal reservoir pore structure characterized by mercury intrusion—a case of southern Junggar basin. *Coal Geology of China*, 30, 29–33.
- Li, Y., Zhang, C., Tang, D., Gan, Q., Niu, X., Wang, K., & Shen, R. (2017). Coal pore size distributions controlled by the coalification process: An experimental study of coals from the Junggar, Ordos and Qinshui basins in China. *Fuel*, 206, 352–363.
- Liu, G., Wang, J., Wei, C., Song, Y., Yan, G., Zhang, J., & Chen, G. (2018a). Pore fractal model applicability and fractal characteristics of seepage and adsorption pores in middle rank tectonic deformed coals from the Huaibei coal field. *Journal of Petroleum Science and Engineering*, 171, 808–817.
- Liu, H., Bai, Y., Bu, J., Li, S., Yan, M., Zhao, P., & Qin, L. (2020). Comprehensive fractal model and pore structural features of medium- and low-rank coal from the Zhunnan coalfield of Xinjiang, China. *Energies*, 13, 7.
- Liu, Y., Zhu, Y., Liu, S., Chen, S., Li, W., & Wang, Y. (2018b). Molecular structure controls on micropore evolution in coal vitrinite during coalification. *International Journal of Coal Geology*, 199, 19–30.
- Liu, Y., Qin, Y., Ma, D., & Duan, Z. (2021). Pore structure, adsorptivity and influencing factors of high-volatile bituminous coal rich in inertinite. *Fuel*, 293, 120418.
- Peng, C., Zou, C., Yang, Y., Zhang, G., & Wang, W. (2017). Fractal analysis of high rank coal from southeast Qinshui basin by using gas adsorption and mercury porosimetry. *Journal of Petroleum Science and Engineering*, 156, 235–249.
- Ren, P., Xu, H., Tang, D., Li, Y., Chen, Z., Sun, C., Zhang, F., Chen, S., Xin, F., & Cao, L. (2019). Pore structure and fractal characterization of main coal-bearing synclines in western Guizhou, China. *Journal of Natural Gas Science and Engineering*, 63, 58–69.
- Shao, L., Li, J., Wang, S., Hou, H., Li, J., & Zhu, M. (2020). Pore structures and fractal characteristics of liquid nitrogen adsorption pores in lignite in the Hailar Basin. *Natural Gas Industry*, 40, 15–25.
- Shi, X., Zheng, Y., Lei, Y., Xue, W., Yan, G., Liu, X., Cai, B., Tong, D., & Wang, J. (2021). Air quality benefits of achieving carbon neutrality in China. *Science of The Total Environment*, 795, 148784.
- Sing, K. S. W., Everett, D. H., Haul, R. A. W., Moscou, L., Pierotti, R. A., Rouquerol, J., & Siemieniewska, T. (1985). Reporting physisorption data for gas/solid systems with special reference to the determination of surface area and porosity. *Pure and Applied Chemistry*, 57, 603–619.
- Sun, B., Yang, Q., Zhu, J., Shao, T., Yang, Y., Hou, C., & Li, G. (2020). Pore size distributions and pore multifractal characteristics of medium and low-rank coals. *Science Reports*, 10, 22353.
- Tao, S., Chen, S., Tang, D., Zhao, X., Xu, H., & Li, S. (2018a). Material composition, pore structure and adsorption capacity of low-rank coals around the first coalification jump: A case of eastern Junggar Basin, China. *Fuel*, 211, 804–815.
- Tao, S., Zhao, X., Tang, D., Deng, C., Meng, Q., & Cui, Y. (2018b). A model for characterizing the continuous distribution of gas storing space in low-rank coals. *Fuel*, 233, 552–557.
- Wang, B., Qin, Y., Shen, J., & Wang, G. (2017a). Summarization of geological study on low rank coalbed methane in China. *Coal Science and Technology*, 45, 170–190.
- Wang, A., Wei, Y., Yuan, Y., Li, C., Li, Y., & Cao, D. (2017b). Coalbed methane reservoirs' pore-structure characterization of different macrolithotypes in the southern Junggar Basin of Northwest China. *Marine and Petroleum Geology*, 86, 675–688.
- Wang, B., Qin, Y., Shen, J., Zhang, Q., & Wang, G. (2018). Pore structure characteristics of low- and medium-rank coals and their differential adsorption and desorption effects. *Journal of Petroleum Science and Engineering*, 165, 1–12.
- Wei, P., Liang, Y., Zhao, S., Peng, S., Li, X., & Meng, R. (2019). Characterization of pores and fractures in soft coal from the No.5 soft coalbed in the Chenghe mining area. *Processes*, 7, 13.
- Wu, F., Huang, N., Liu, G., Niu, L., & Qiao, Z. (2020). Pathway optimization of China's carbon emission reduction and its provincial allocation under temperature control threshold. *Journal of Environmental Management*, 271, 111034.
- Wu, J., Tang, D., Li, S., & Ren, P. (2017). Characteristics and influence factors of pore structure of coal reservoirs in the eastern margin of Ordos basin. *Coal Geology & Exploration*, 45, 58–65.
- Xie, H., Ni, G., Li, S., Sun, Q., Dong, K., Xie, J., Wang, G., & Liu, Y. (2019). The influence of surfactant on pore fractal characteristics of composite acidized coal. *Fuel*, 253, 741–753.
- Xie, J., Xie, J., Ni, G., Rahman, S., Sun, Q., & Wang, H. (2020). Effects of pulse wave on the variation of coal pore structure in pulsating hydraulic fracturing process of coal seam. *Fuel*, 264, 116906.
- Xin, F., Xu, H., Tang, D., Yang, J., Chen, Y., Cao, L., & Qu, H. (2019). Pore structure evolution of low-rank coal in China. *International Journal of Coal Geology*, 205, 126–139.
- Xu, S., Hu, E., Li, X., & Xu, Y. (2020). Quantitative analysis of pore structure and its impact on methane adsorption capacity of coal. *Natural Resources Research*, 30, 605–620.
- Xu, X., Meng, Z., & Wang, Y. (2019). Experimental comparisons of multiscale pore structures between primary and disturbed coals and their effects on adsorption and seepage of coalbed methane. *Journal of Petroleum Science and Engineering*, 174, 704–715.
- Yan, Z., Wang, J., & Wang, X. (2021). Sedimentary environments and coal accumulation of the Middle Xishanyao Formation, Jurassic, in the Western Dananhu Coalfield, Turpan-Hami Basin. *Geofluids*, 2021, 6034055.

- Yang, Y., Liu, X., Zhao, W., & Wang, L. (2019). Intrinsic relationship between Langmuir sorption volume and pressure for coal: Experimental and thermodynamic modeling study. *Fuel*, *241*, 105–117.
- Yao, Y., Liu, D., Tang, D., Tang, S., & Huang, W. (2008). Fractal characterization of adsorption-pores of coals from North China: An investigation on CH<sub>4</sub> adsorption capacity of coals. *International Journal of Coal Geology*, *73*, 27–42.
- Yu, S., Bo, J., Pei, S., & Wu, J. (2018). Matrix compression and multifractal characterization for tectonically deformed coals by Hg porosimetry. *Fuel*, *211*, 661–675.
- Yu, Y., & Wang, Y. (2020). Characteristics of low-rank coal reservoir and exploration potential in Junggar Basin: New frontier of low-rank CBM exploration in China. *Journal of Petroleum Exploration and Production Technology*, *10*, 2207–2223.
- Yuan, M., Lyu, S., Wang, S., Xu, F., & Yan, X. (2022). Macrolithotype controls on natural fracture characteristics of ultra-thick lignite in Erlan Basin, China: Implication for favorable coalbed methane reservoirs. *Journal of Petroleum Science and Engineering*, *208*, 109598.
- Yue, J., Wang, Z., Chen, J., Zheng, M., Wang, Q., & Lou, X. (2019). Investigation of pore structure characteristics and adsorption characteristics of coals with different destruction types. *Adsorption Science & Technology*, *37*, 623–648.
- Zhang, K., Cheng, Y., Li, W., Hao, C., Hu, B., & Jiang, J. (2019). Microcrystalline characterization and morphological structure of tectonic anthracite using XRD, liquid nitrogen adsorption, mercury porosimetry, and micro-CT. *Energy & Fuels*, *33*(11), 10844–10851. <https://doi.org/10.1021/acs.energyfuels.9b02756>.
- Zhang, M., Duan, C., Li, G., Fu, X., Zhong, Q., Liu, H., & Dong, Z. (2021). Determinations of the multifractal characteristics of the pore structures of low-, middle-, and high-rank coal using high-pressure mercury injection. *Journal of Petroleum Science and Engineering*, *203*, 108656.
- Zhang, S., Tang, S., Tang, D., Yan, Z., Zhang, B., & Zhang, J. (2009). Fractal characteristics of coal reservoir seepage pore, east margin of Ordos Basin. *Journal of China University of Mining & Technology*, *38*, 713–718.
- Zhang, S., Tang, S., Tang, D., Huang, W., & Pan, Z. (2014). Determining fractal dimensions of coal pores by FHH model: Problems and effects. *Journal of Natural Gas Science and Engineering*, *21*, 929–939.
- Zhou, S., Liu, D., Cai, Y., Yao, Y., Che, Y., & Liu, Z. (2017a). Multi-scale fractal characterizations of lignite, subbituminous and high-volatile bituminous coals pores by mercury intrusion porosimetry. *Journal of Natural Gas Science and Engineering*, *44*, 338–350.
- Zhou, S., Liu, D., Cai, Y., & Yao, Y. (2016). Fractal characterization of pore-fracture in low-rank coals using a low-field NMR relaxation method. *Fuel*, *181*, 218–226.
- Zhou, S., Liu, D., Karpyn, Z. Y., Cai, Y., & Yao, Y. (2018). Effect of coalification jumps on petrophysical properties of various metamorphic coals from different coalfields in China. *Journal of Natural Gas Science and Engineering*, *60*, 63–76.
- Zhou, S., Liu, D., Cai, Y., & Yao, Y. (2017b). Effects of the coalification jump on the petrophysical properties of lignite, subbituminous and high-volatile bituminous coals. *Fuel*, *199*, 219–228.
- Zhu, Y., Wang, Y., Chen, S., Zhang, H., & Fu, C. (2016). Qualitative-quantitative multiscale characterization of pore structures in shale reservoirs: A case study of Longmaxi Formation in the Upper Yangtze area. *Earth Science Frontiers*, *23*, 154–163.
- Zhu, Q., Yang, Y., Lu, X., Liu, D., Li, X., Zhang, Q., & Cai, Y. (2019). Pore structure of coals by mercury intrusion, N<sub>2</sub> adsorption and NMR: A comparative study. *Applied Sciences-Basel*, *9*, 1680.